# Facile co-sintering process for fabrication of sustainable antifouling AgNPs-enhanced tight ceramic ultrafiltration membranes for protein separation

*Dong Zou [a], Xianfu Chen [a], Enrico Drioli [b], Xuebin Ke [c], Minghui Qiu [a], Yiqun Fan [a,]**

[a] State Key Laboratory of Materials-Oriented Chemical Engineering, College of Chemical Engineering, Nanjing Tech University, Nanjing 210009, P. R. China

[b] Institute on Membranes and Modelling of Chemical Reactors, CNR, and Department of Chemical Engineering and Materials, University of Calabria, 87030 Arcavacata di Rende, CS, Italy

[c] Department of Chemical Engineering, University of Hull, HU6 7RX, United Kingdom

*Corresponding author: Tel.: +86 25 83172277; Fax: +86 25 83172292

E-mail: yiqunfan@njtech.edu.cn

## Abstract

Protein separation in medical care applications using tight ceramic ultrafiltration (UF) membranes with multilayer asymmetric structures is hindered by challenges in their fabrication and fouling phenomenon. In this study, a facile co-sintering method for fabrication of silver nanoparticles (AgNPs)-enhanced tight ceramic ultrafiltration membranes was comprehensively investigated. The introduction of AgNPs into the membrane layer not only controlled the membrane surface charge properties, but also alleviated the sintering stress in the co-sintering process, ensuring a complete membrane layer owing to the higher ductility. The AgNPs obtained from silver nitrate were introduced before the formation of boehmite nucleation, providing a uniform distribution of AgNPs within boehmite owing to the electric double layer. The final UF membranes prepared by the co-sintering process exhibited a molecular weight cut-off of 9000 Da and permeability of 62 $Lm^{-2}h^{-1}bar^{-1}$. Furthermore, the isoelectric point of the membrane surface could be controlled by the AgNPs (from 9.0 to 2.7 unit?), providing sustainable antifouling properties for protein purification owing to the electrostatic repulsion force. The proposed facile co-sintering process for fabrication of antifouling ceramic UF membranes with the assistance of AgNPs could decrease the sintering time and energy consumption, and thus is promising for industrial protein purification applications.

**Keywords:** AgNPs; tight Ceramic ultrafiltration membranes; Protein purification; Antifouling performance.

# 1. Introduction

Pure proteins attract increasing attention owing to their potential applications in food, nutrition, and medical care [1, 2]. In medical care applications, proteins with high purities have been employed to fight against various diseases [3, 4]. There is a large demand for protein purification. Ceramic tight ultrafiltration (UF) membranes with pore sizes of 2–5 nm have a large potential to separate and purify protein suspensions owing to their excellent chemical and physical stabilities and long operational lifetimes. However, the membrane fouling hinders the wide application of tight ceramic UF membranes. Conventionally, ceramic membrane materials are often composed of $ZrO_2$, $Al_2O_3$, $TiO_2$, and their mixtures [5]. These materials do not exhibit satisfactory antifouling performances while treating protein solutions. The membrane fouling phenomenon may lead to a significant flux decrease, increased energy demand, high operational cost, shorter operational lifetime, and additional labor for maintenance. Therefore, the development of a high-performance ceramic membrane material with a satisfactory protein antifouling performance is essential. In order to alleviate the membrane fouling, various approaches have been employed to modify the membrane surface charge [6], hydrophilicity–hydrophobicity performance [7], surface roughness [8, 9], inhomogeneous pore size distribution [10], etc.

Nanoparticles (NPs)-enhanced membranes with various functionalities have been proposed as high-performance antifouling membranes to separate and purify waste water [11, 12]. NPs consisting of various materials, such as zeolites, $TiO_2$, ZnO, $ZrO_2$ [13-15], Ag, Au, and Pd [16, 17], have been introduced to modify the properties of ceramic and polymer membranes, providing better antifouling performances and stable chemical properties. Among the nanoparticles, Ag nanoparticles (AgNPs) attract significant attention owing to the enhancement in the antimicrobial activity [18, 19] and low toxicity toward mammalian cells for long-term applications. Most studies have been focused on the antimicrobial properties as well as the optical and electrical performances [20, 21]. These studies confirmed that the surface of the AgNPs-enhanced material could alleviate the adhesion between the membrane surface and bacteria with a controlled release of $Ag^+$, which paves the way for the design and fabrication of self-cleaning antimicrobial surfaces. For example, Mecha et al. [22] fabricated an AgNPs-modified woven fabric microfiltration membrane and investigated a potable water treatment using such membranes. The membranes exhibited a satisfactory disinfection performance for a raw river water.

Furthermore, the nanoscale AgNPs exhibit other valuable properties such as a negative zeta potential [23], higher toughness, and tensile ductility [24]. If the AgNPs with these properties are embedded in ceramic membrane materials, such membranes could have controllable surface charge properties and a facile thermal treatment in the fabrication process. Tang et al. [23, 25, 26] carried out a series of studies on negatively AgNPs charged organic membranes using a nanotemplate approach and reported that the AgNPs (negatively charged) modified the surface properties of the composite nanofiltration membranes. They exhibited satisfactory separation performances for treatment of a NaCl/$MgSO_4$ solution, as the AgNPs could provide surface oxidation, generating negative charges. In addition, the AgNPs could attract ions (e.g., $Cl^-$) on the

membrane surface, inducing a more negative surface. These studies pave the way for the design and fabrication of high-performance ceramic membrane materials with controllable surface charges. Furthermore, Lin et al. [27, 28] reported the effect of AgNPs doping on the thermal treatment of ceramic membranes at high temperatures. They fabricated $TiO_2$/Ti composite microfiltration (MF) and UF membranes using AgNPs to alleviate the sintering stress and thermal expansion mismatch between the metal support and $TiO_2$ layer, efficiently preventing membrane cracks in the sintering process. They also explained the toughening mechanism using AgNPs to overcome the mismatch in the sintering process owing to their higher toughness performances, providing a good approach to fabricate integrated ceramic membrane layers at high temperatures.

Although the AgNPs have various advantages for the fabrication of ceramic membranes, the AgNPs having a higher surface energy could easily aggregate and thus affect the integrity of the membrane surface and reduce the antifouling efficiency if they are simply mixed or directly coated on the membrane surface. It is challenging to disperse the AgNPs by conventional methods, such as sonication and grinding [29], owing to the strong intraparticle interactions. Therefore, it is crucial to develop an effective method to disperse the AgNPs in the composite membranes. Zhang et al. [30] proposed a novel approach to modify the membrane surface by a simultaneous grafting of AgNPs and sulfobetaine methacrylate. The AgNPs were uniformly distributed on the membrane surface and exhibited a better antifouling performance. Das et al. [31] developed a green method to load AgNPs on a silica surface by coating a protein to fabricate a stable composite material. The AgNPs were distributed uniformly in the designed material. Basri et al. [32] investigated mainly the effects of polyvinylpyrrolidone and triaminopyrimidine on the silver dispersion. Their membrane has a good potential for antibacterial applications. In addition, silane coupling agents can reduce the degree of hydrophilicity and surface energy of the particles and effectively prevent agglomeration [33, 34].

In this study, we utilized the advantages of AgNPs with good toughness properties and negative surface charges to design a high-performance ceramic tight membrane with a controllable surface charge by co-sintering process. The AgNPs not only relieved the stress and smoothened the membrane surface in the co-sintering process, but also controlled the membrane surface charge, providing a better electrostatic repulsion of bovine serum albumin (BSA) molecules. Using $AgNO_3$, AgNPs were introduced to prepare a uniform AgNPs-doped boehmite sol. The $AgNO_3$ was in-situ reduced into the AgNPs in the boehmite sol with the aid of alcohol and appropriate thermal treatment. Parameters, such as the distribution of AgNPs within boehmite sol, rejection performance, flux, and antifouling performance, were investigated to fabricate a ceramic tight UF membrane with a satisfactory antifouling performance. The use of co-sintering technology, a facile and low-cost methodology [35, 36] significantly reduced the fabrication period and energy consumption.

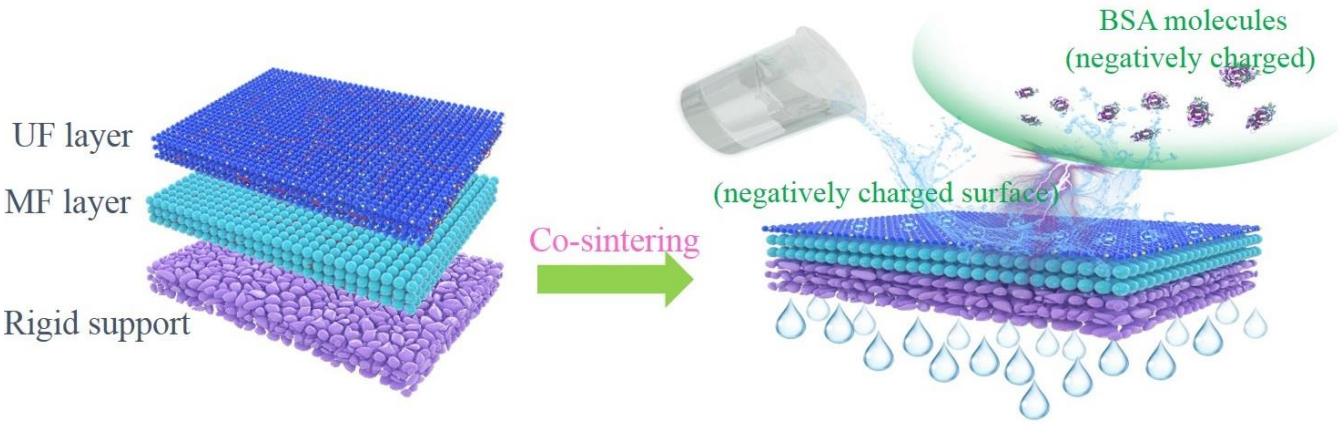


**Fig. 1** Illustrations of the fabrication of the flat ceramic tight UF membrane and separation to purify a protein solution.

## 2. Experimental methods

### 2.1 Materials

Al-tri-sec-butoxide, silver nitrate ($AgNO_3$), and glycerol were purchased from Sigma-Aldrich. Alcohol, acetic acid, and BSA were purchased from Shanghai Lingfeng Chemical Reagent. Alumina powders used to fabricate a ceramic support (mean particle size of 3000 nm) and MF membrane material (mean particle size of 300 nm) were purchased from Sumitomo, Japan. Deionized water was used in all experiments.

### 2.2 Synthesis of a boehmite sol

**Pure boehmite sol:** Al-tri-sec-butoxide as a precursor was mixed with alcohol to form a homogenous solution. This process could reduce the viscosity of the Al-tri-sec-butoxide and form a homogenous solution with alcohol, beneficial for the subsequent hydrolysis. The homogenous solution was then added into hot water (90 °C) and stirred for 1 h under refluxing. Subsequently, acetic acid was added and the refluxing as well as stirring were continued for another 1 h. Finally, glycerol was added under refluxing and stirring for 1 h. Upon cooling to room temperature, the sol was successfully prepared [37].

**AgNPs-doped boehmite sol:** The preparation of the AgNPs-doped boehmite was similar to that of the pure boehmite sol. However, before the addition of acetic acid, an $AgNO_3$ solution was added dropwise; the steps are illustrated in **Fig. S1**.

### 2.3 Fabrication of ceramic membranes

Before the fabrication of ceramic UF membranes, flat alumina supports were fabricated and characterized [38, 39]. As shown in **Fig. 2**, no defects were observed on the surface of the alumina support. The support had a mean pore size of ~1 μm, narrow pore size distribution, and permeability of approximately 1700 $Lm^{-2}h^{-1}bar^{-1}$. In addition, the roughness of the support was approximately ~1 μm (**Fig. S2**), which is beneficial to fabricate a ceramic membrane with a high separation accuracy.

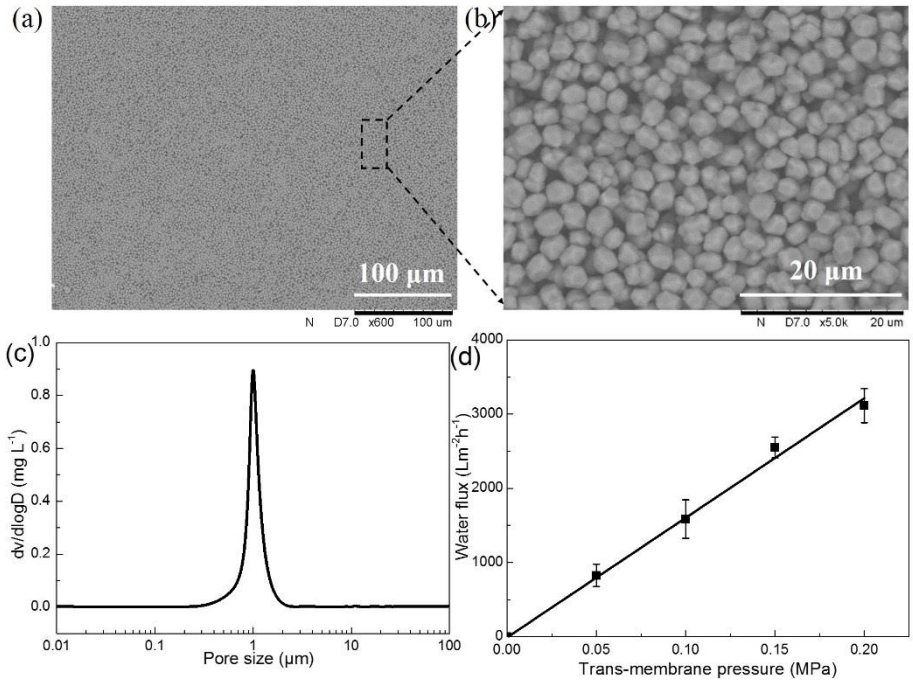


**Fig. 2** Characterizations of the ceramic support: (a) (b) surface of the support, (c) pore size distribution, and (d) water flux.

**Fabrication of an AgNPs-doped ceramic UF membrane (ACUM):** ACUM was fabricated by co-sintering process. An alumina dispersion (its fabrication is presented in our previous report [5]) was dip-coated on the support surface for 60 s. The wet alumina MF membrane was then dried at room temperature (20 to 25 °C) for 12 h and at 70 and 110 °C for 6 h. The AgNPs-doped boehmite sol was coated on the dry MF membrane for 10 s, which was then dried at a relative humidity of 60% and 60 °C for 12 h. The membrane was then placed in an oven at 70 °C and 110 °C for 6 h. Finally, the membrane was co-sintered once at 1000 °C for 2 h, at a heating and sintering rate of 1 °C/min.

**Fabrication of a conventional ceramic UF membrane (CCUM):** CCUM was fabricated by a conventional process, consistent with that of ACUM. In addition, the alumina MF membrane was sintered at 1050 °C. After coating of the pure boehmite sol, the UF membrane was sintered at 1000 °C. This conventional method involved two sintering processes.

### 2.4 Membrane material characterization

The average pore diameter of the fabricated ceramic support was characterized by a mercury porosimetry (Poremaster GT-60, quantachrome) device. The surface microstructure and membrane cross section (along the membrane thickness) were characterized by scanning electron microscopy (SEM, Hitachi, S4800, Japan). The sols with different $AgNO_3$ doping contents were dried and sintered at 1000 °C. The alumina phase compositions of the materials were characterized by X-ray diffraction (XRD, Smart Lab, Rigaku, Japan). The roughness of the membrane surfaces with and without doping AgNPs were measured by atomic force microscopy to produce two- and three-dimensional images. The pore diameter, pore volume, and surface area of the membrane material with different $AgNO_3$ doping contents were measured by the Brunauer–Emmett–Teller method (BET, BELSORP Mini). The binding energy of the membrane material was measured by X-ray photoelectron spectroscopy

(XPS, Thermo ESCALAB 250, USA). All binding energies were referenced to 285.0 eV corresponding to the C 1*s* peak. The zeta potentials of the boehmite sols were measured using the dynamic light scattering technique (Zeta PALS, Brookhaven, USA). The bonding strength between the MF and UF membrane layers was measured by a nanoscratch tester (NANO TEST, MML) to evaluate the difference between the conventional and co-sintering processes. The porosity of the ceramic tight UF membrane was characterized by an ellipsometry device (Complete EASEM-2000U, J.A. Woollam, **Fig. 3**) by measuring the refractive index and using the following equation [40-42]:

$$f_a \frac{n_a^2 - n_{eff}^2}{n_a^2 + 2n_{eff}^2} + (1 - f_a) \frac{n_b^2 - n_{eff}^2}{n_b^2 + 2n_{eff}^2} = 0 \quad (1)$$

where $f_a$ is the porosity of the UF membrane layer, $n_a$ is the refractive index of the pores, and $n_{eff}$ is the effective index [43]. To demonstrate the rationality of ellipsometry for the porosity measurement of the membrane surface, three different angles, from 65° to 75°, were used to measure the correlation between the experimental and model data. As shown in **Fig. 3**, the generated and experimental data exhibit a good quality of fitting at wavelengths in the range of 600 to 1000 nm.

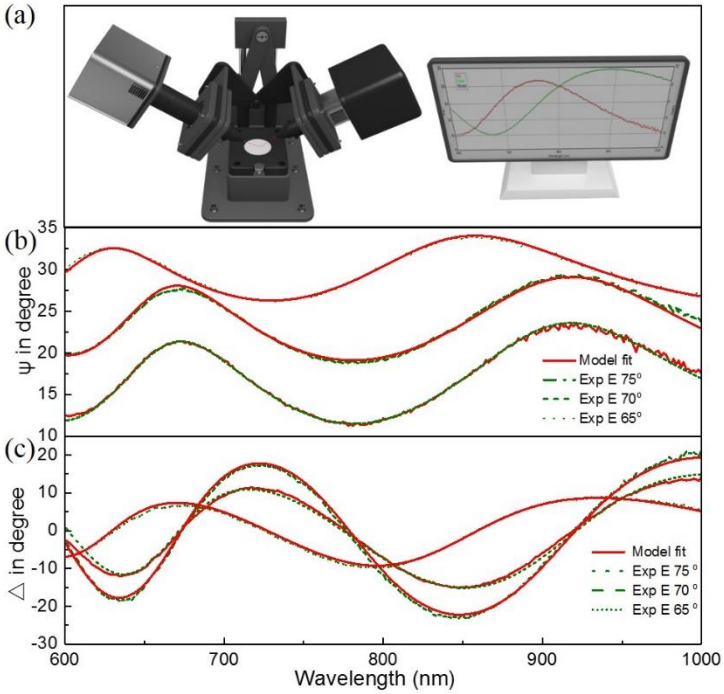


**Fig. 3** (a) Ellipsometry device and (b) (c) ellipsometry analysis of $\psi$ and $\Delta$ of the membrane surface.

**2.5 Separation and antifouling properties of the UF membranes**

The pure water flux, permeate flux, and permeability were characterized by a cross-flow apparatus (the structure of the apparatus is presented in our previous report [42]). The rejection performances of ACUM and CCUM were characterized by a dextran solution. The mean pore sizes could be calculated using the rejection rates. The total content of the dextran solution was approximately 6.5 g/L, with 10000 Da (2.5 g/L), 40000 Da (1 g/L), 70000 Da (1 g/L), and 500000 Da (2 g/L). The concentrations of the dextran solutions before and after the membrane were characterized by gel permeation chromatography (Waters Corp., USA). The flux and permeability were calculated by:

$$J = \frac{V}{A \cdot t \cdot P} \quad (2)$$

$$Q = \frac{V}{A \cdot t} \quad (3)$$

where $J$ is the permeability of the membrane or support ($Lm^{-2}h^{-1}bar^{-1}$), $Q$ is the pure water flux or permeate flux ($Lm^{-2}h^{-1}$), $V$ is the permeate volume (mL), $A$ is the effective membrane surface area ($m^2$), $t$ is the filtration time (h), and $P$ is the trans-membrane pressure (bar). The antifouling performances of ACUM and CCUM were characterized by separation of a protein (BSA) solution. The rejection of BSA was calculated by:

$$R = \frac{C_f - C_p}{C_f} \quad (4)$$

where $R$ is the rejection performance, and $C_f$ and $C_p$ are the concentrations of the feed and permeate solutions of BSA, respectively. The feed and permeate solutions were then analyzed by ultraviolet spectroscopy (Nanodrop 2000C, Thermo Scientific, USA) at the required wavelength of BSA. The antifouling performance of the membrane was measured using the reported method [44]. ACUM and CCUM were used to treat pure water and BSA solution (0.5 g/L) for three cycles. At the end of each cycle, the membrane was thoroughly washed with pure water. After three cycles of BSA filtration, the pure water permeabilities of ACUM and CCUM were measured and denoted as $J_4$ ($Lm^{-2}h^{-1}bar^{-1}$). The original pure water permeabilities of the membranes were measured and denoted as $J_1$ ($Lm^{-2}h^{-1}bar^{-1}$). The flux recovery ratio (FRR) was calculated by:

$$FRR = \frac{J_4}{J_1} \quad (5)$$

# 3. Results and discussion

### 3.1 Investigation of the stable performance of the AgNPs-doped boehmite sols

AgNPs have a higher surface energy and easily agglomerate in a simple mixing process, leading to instability and inhomogeneity of the sol. The inhomogeneous size distributions of AgNPs hindered the investigation of structure–property relationships of a composite membrane [11]. Therefore, a uniform dispersivity of the AgNPs in the boehmite sol is required. **Fig. 4a** shows the zeta potentials of the boehmite sols with and without doped AgNPs as a function of the aging time. The zeta potentials were all maintained around 30 mV with the increase of the aging time, indicating that the AgNPs did not affect the stability of the boehmite sol. The AgNPs-doped and pure boehmite sols are shown in **Fig. 4a** (insets). The AgNPs-doped boehmite sol was brown–yellow, as the in-situ-formed AgNPs exhibited surface plasmon resonance [45, 46]. **Fig. 4b** shows the relationships between pH and zeta potential for the AgNPs and AlOOH. The AgNPs are negatively charged, while AlOOH is positively charged at a pH of 3–4 (the pH of the boehmite sol is presented in our previous report [37]). Therefore, the AgNPs reduced from the silver nitrate during the thermal treatment [47] could be absorbed around the crystal nucleus of boehmite with the aid of glycerol, forming a stable system owing to the electric double-layer (EDL) effect. This could stabilize

the AgNPs in the boehmite sol and form a uniform AgNPs-doped sol. With this approach, giant networks of the organic additives and AgNPs could be formed, effectively constraining the agglomeration of AgNPs and simultaneously controlling the particle size at the nanoscale (**Fig. 4c**). **Fig. 4d** shows the thermal process used for the AgNPs-doped boehmite sol. The sol was formed into a gel with water evaporation. After sintering at 1000 °C, the AgNPs could be uniformly loaded on the membrane surface.

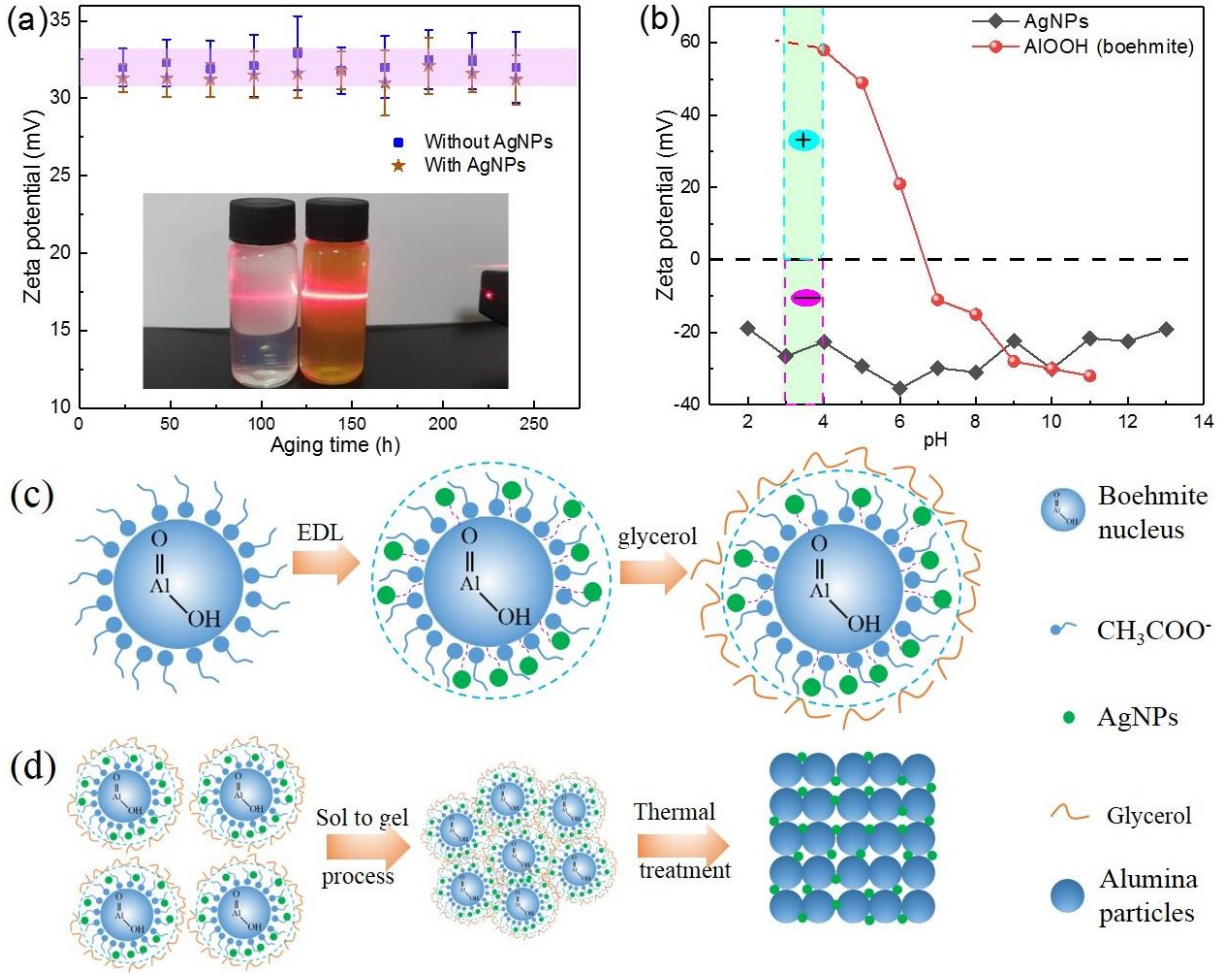


**Fig. 4** Dispersivity performances of the AgNPs and boehmite. (a) Zeta potentials of the boehmite sols (with and without AgNPs) as a function of the aging time. (b) Zeta potentials of the AgNPs and AlOOH (the isoelectric point (IEP) of the boehmite is presented in the Wu's report [48]). Schematics of the (c) dispersion process and (d) thermal treatment of ACUM.

### 3.2 Effect of the silver nitrate doping content on the microstructure of membrane material

In our previous study [37], the boehmite sol was synthetized to prepare γ-$Al_2O_3$ nanofiltration membranes and parameters such as $[H^+]/[Al^+]$ and $[H_2O]/[Al^+]$ were investigated. Usually, the doping method using AgNPs into the membrane layer could significantly affect the pore volume and surface area, and thus the permeability performance. The effect of the doping content of $AgNO_3$ is discussed to characterize the microstructure of the AgNPs-doped alumina material by the BET method. **Fig. 5a** shows the surface area and pore volume. The surface area and pore volume decreased with the increase in the AgNPs doping content, as the AgNPs filled the pores of the alumina material, which improved its nonporous components and

decreased the pore volume and specific surface area. The decreases in the pore volume and specific surface area could reduce the permeability performance of the final membrane material. **Fig. 5b** shows that the pore diameter increased with the AgNPs doping content particularly in the range of 10 to 20 wt.%, as the AgNPs tended to connect with each other in the sintering process, which accelerated the growth of AgNPs and increased their diameters. Furthermore, when the doping content increased from 0 to 20 wt.%, the AgNPs could accelerate the alumina phase transition from $\gamma$ to $\alpha$ (**Fig. 5c**), which is indicative of a rapid increase in the alumina particle diameter [5]. The alumina phase transition could also be responsible for the decreased specific surface area (**Fig. 5a**) and increased pore diameter (**Fig. 5b**).

**Figs. 5d–f** show the microstructure evolution with the AgNPs doping content by SEM images of the membrane surfaces. The membrane surface with 5 wt.% of AgNPs was smooth without obvious defects. However, the membrane surfaces with higher AgNPs doping contents were different, particularly at 10 and 20 wt.%. A large number of larger pores were observed on the membrane surface (**Figs. 5e** and **5f**), which is consistent with our previous study (inhomogeneous nucleation of α-alumina at high temperatures [7]). This could be attributed to two factors. First, the high content of AgNPs could lead to a uniform and unstable dispersion of AgNPs among the boehmite with excess AgNPs on the local membrane surface. Second, the AgNPs doping could promote the alumina phase transition, from γ to α phase, and thus promote the growth of the alumina crystal, thereby enlarging the local membrane pores. Furthermore, it is worth noting that if the AgNPs were not doped into the boehmite sol, the membrane surface could have significant cracks formed during the co-sintering process (**Fig. S3**). The mismatch in thermodynamic properties between the MF and UF layers in the co-sintering process and larger tensile stress from the UF layer could lead to cracks [5]. However, as discussed above, the membrane surface with doped AgNPs (5 wt.%) was smooth without defects. The AgNPs with the high ductility and toughness could absorb and deflect the stress, providing a membrane surface with a high integrity, which is consistent with our previous study [49]. Overall, the AgNPs doping content in this work was controlled at 5 wt.%.

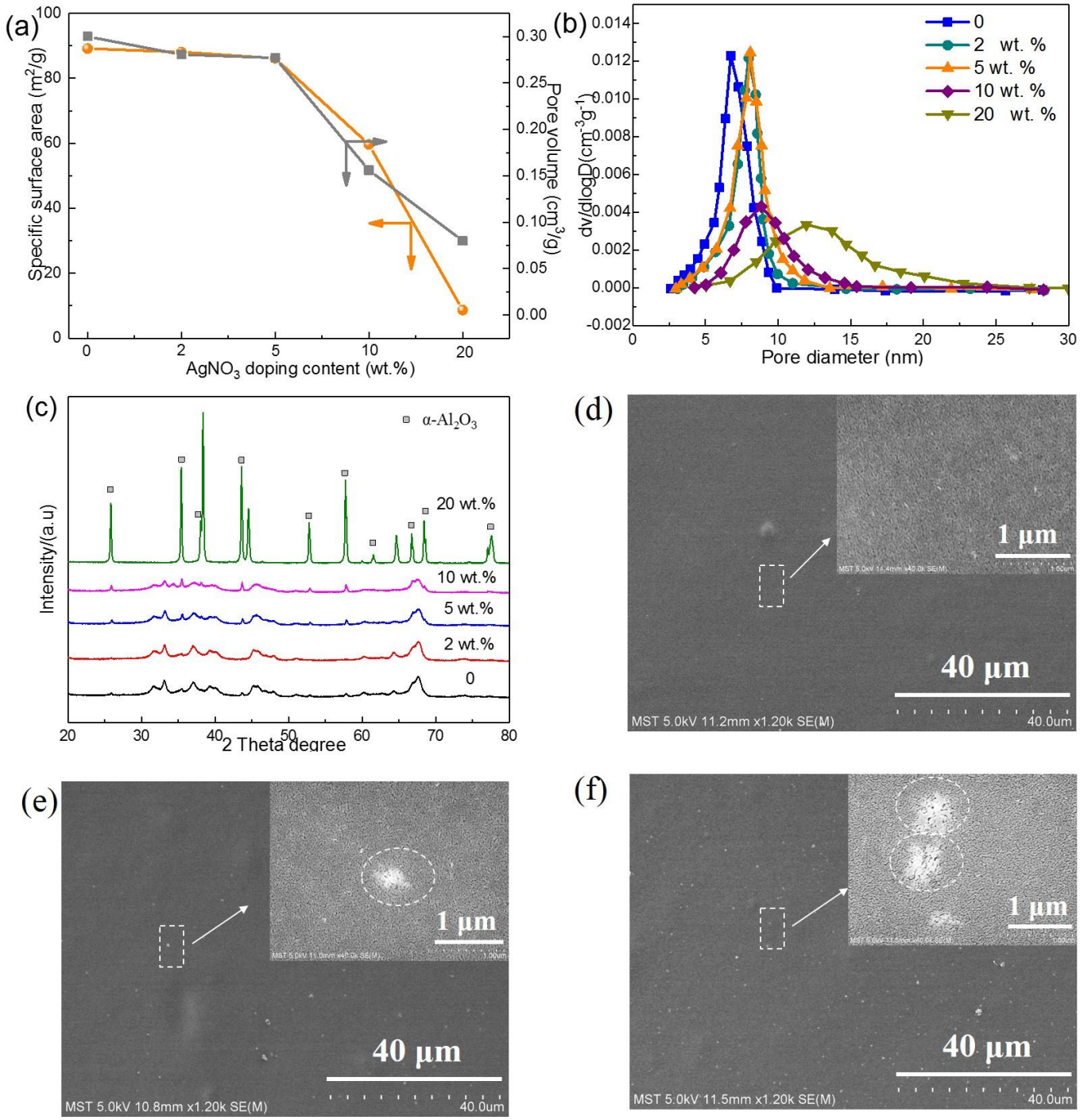


**Fig. 5** Microstructure of the AgNPs-doped alumina material: (a) specific surface area and pore volume, (b) pore diameter, (c) alumina phase transition for different AgNPs loadings, and membrane surface microstructures for different AgNPs doping contents of (d) 5 wt.%, (e) 10 wt.%, and (f) 20 wt.%.

### 3.3 Physicochemical properties of the AgNPs-doped $Al_2O_3$ materials

As discussed above, the dispersivity of the AgNPs in the boehmite sol had an important role in the fabrication of the ceramic UF membrane with a higher integrity. The sample of $Al_2O_3$ with 5 wt.% of $AgNO_3$ was investigated in detail by energy-dispersive X-ray spectroscopy mapping after sintering at 1000 °C (**Fig. 6**). The elements, Al, O, and Ag, were homogeneously distributed, which confirmed that the AgNPs well dispersed within the alumina particles. Transmission electron microscopy (TEM) images at high magnifications were acquired to observe the microstructure of the AgNPs. Using

the images in **Figs. 6e** and **6f**, the sizes of the AgNPs and alumina particles were precisely characterized. The sizes of the AgNPs were approximately 5 nm, while the lattice plane spacing was approximately 0.34 nm, consistent with the previous report [28].

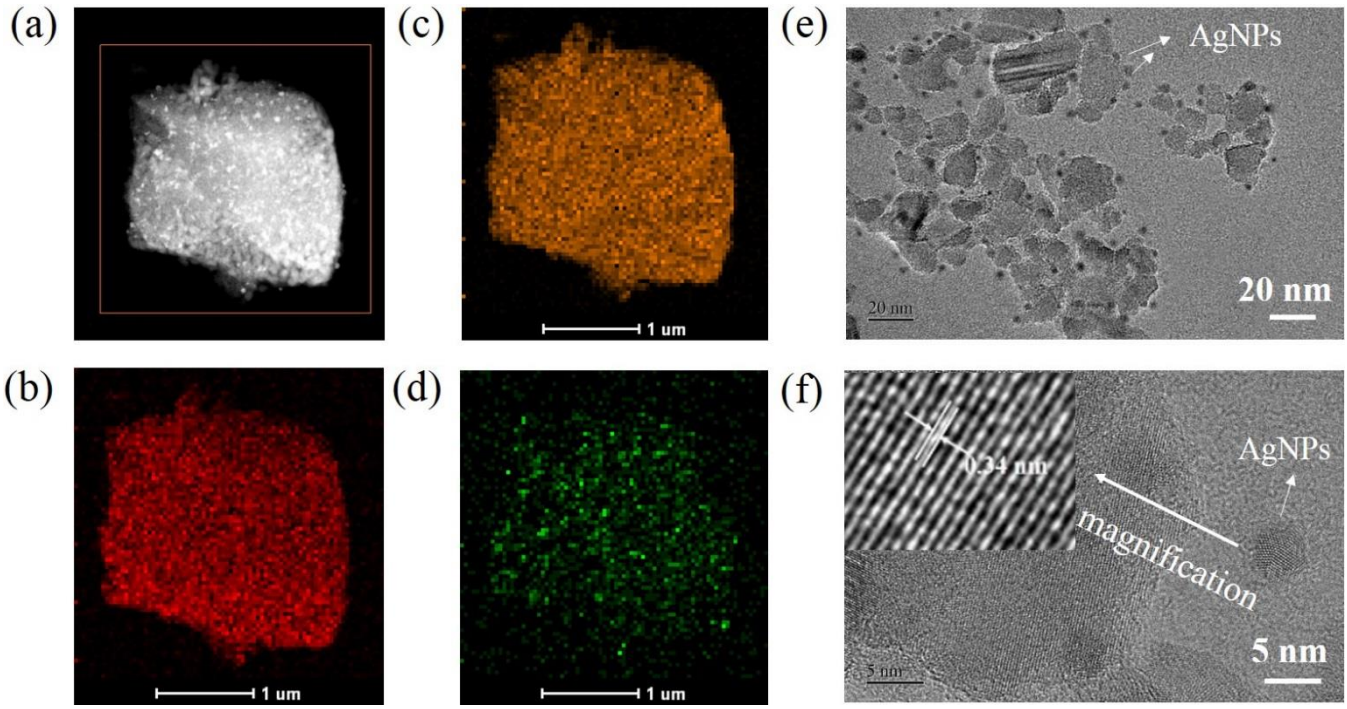


**Fig. 6** Microstructure of the AgNP-doped alumina material: (a)–(d) elemental distributions and (e) (f) TEM images.

An XPS characterization was carried out to analyze the valence states of the AgNPs-doped alumina materials after sintering at 1000 °C for 2 h. **Fig. 7** shows the binding energies referenced to a carbon contaminant (C 1*s*, 284.6 eV). The full spectrum is presented in **Fig. 7a**. Ag 3*d* peaks were observed after the AgNPs doping, in addition to the major peaks of O 1*s* and Al 2*p*. **Fig. 7b** shows a fine Ag spectrum with peaks of Ag $3d_{5/2}$ and Ag $3d_{3/2}$. The XPS experimental results were fitted, yielding peaks of Ag and $Ag_2O$. The Ag $3d_{5/2}$ peak was deconvoluted to two major peaks at 367.8 eV (Ag) and 368.4 eV ($Ag_2O$) [28], while the peak at 374.2 eV corresponds to Ag metal [50]. Ag and $Ag_2O$ could be simultaneously present in the material, though Ag was dominant. **Fig. 7c** shows that the binding energy of Al 2*p* of the material doped with $AgNO_3$ (74.18 eV) was higher than that of the material without doping (73.88 eV). This indicates that the AgNPs could be partly introduced substitutionally, providing a slight increase in the $V_{Al}'''$ concentration and thus a lower electronic cloud density [7]. This demonstrates that the Al–O–Ag chemical bonds are formed [51-53] between the alumina particles and AgNPs.

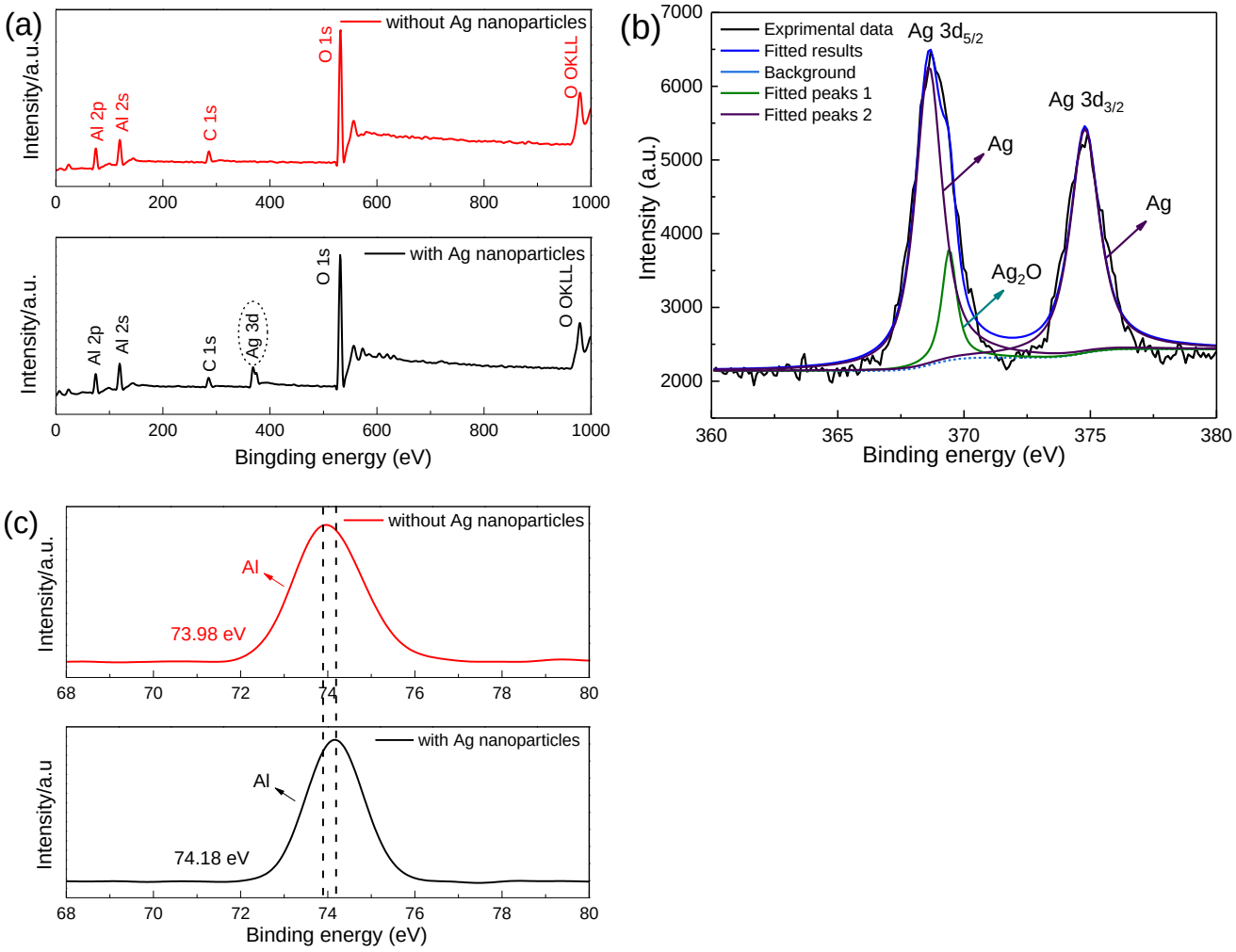


**Fig. 7** XPS spectra of the alumina materials with and without the $AgNO_3$ doping: (a) survey, (b) Ag, and (c) Al.

### 3.4 Characterization of the ceramic UF membranes

#### 3.4.1 Microstructures of ACUM

The SEM image (**Fig. 8a**) shows that the surface of ACUM was defect-free; the pore structure on the membrane surface was not clearly observed at a lower magnification. The flat ACUM is shown in **Fig. 8a** (**inset**). A green–red optical opalescence is observed, which is consistent with the Kuzniatsova's study [54], where the phenomenon was attributed to the relationship between the membrane thickness and color distribution. The membrane pore structure could be observed at a higher magnification (**Fig. 8a-1**). **Fig. 8b** shows the cross-section structure of ACUM including the ceramic support, MF layer, and UF layer (from left to right). The thicknesses of the MF and UF membrane layers were ~40 μm and ~1 μm, respectively.

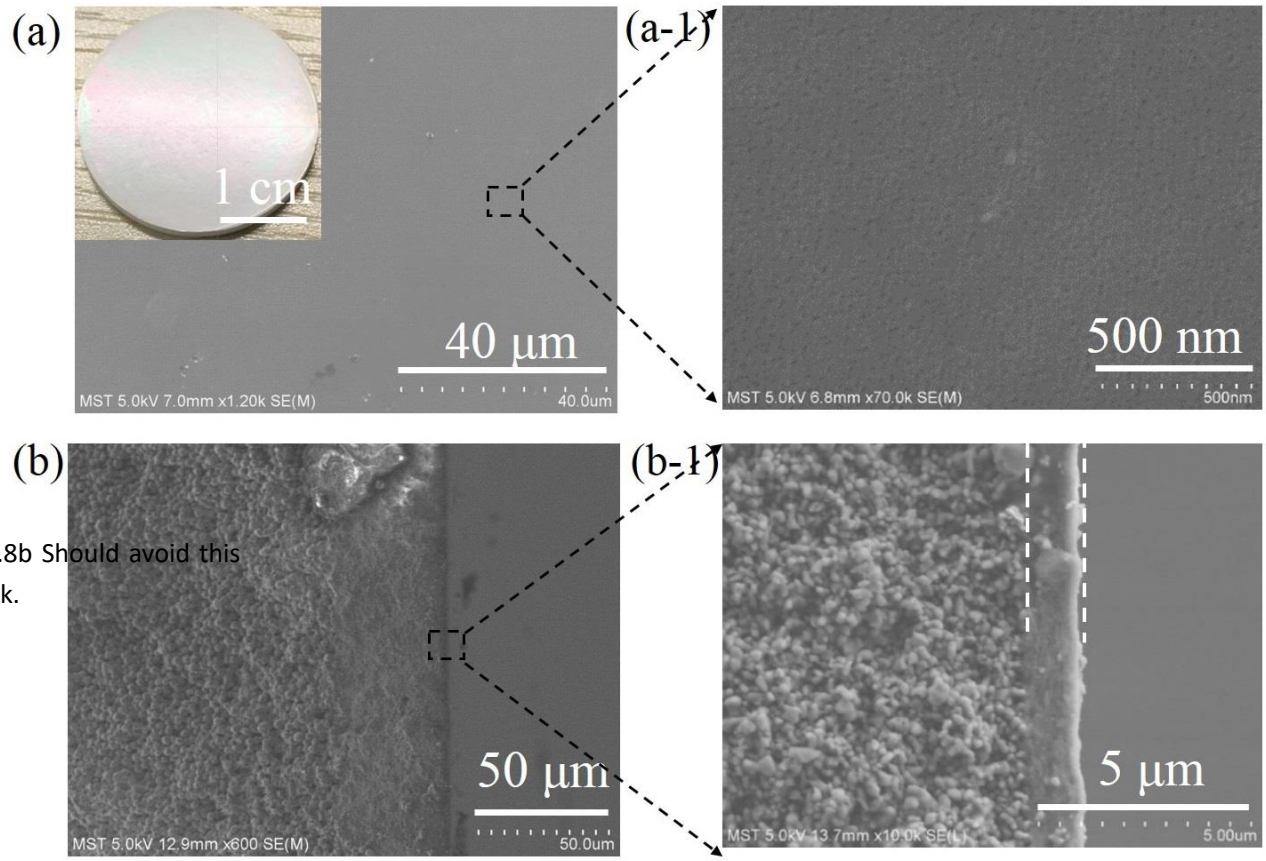


Fig.8b Should avoid this bulk.

**Fig. 8** Microstructure of the ceramic UF membrane: (a) (a-1) surface and (b) (b-1) cross section.

### 3.4.2 Comparison of the pore size distributions and permeability performances of CCUM and ACUM

The dextran rejection performances of ACUM and CCUM are compared in **Fig. 9.** The molecular weight cut-offs (MWCOs) of ACUM and CCUM were 9000 and 10800 Da, respectively. The dextran rejection performances and Equations 6 and 7 were used to calculate the pore size distributions:

$$r_p = 0.33 M_w^{\,0.46} \tag{6}$$

$$\varphi(r_p) = \frac{1}{r_p \sigma_p \sqrt{2\pi}} \exp\left(-\frac{[\ln(r_p) - \mu_p]^2}{2\sigma_p^2}\right) \tag{7}$$

where $M_w$ is the MWCO (Da), $r_p$ is the effective pore radius (nm), $\mu_p$ is the mean effective pore size, and $\sigma_p$ is the geometric standard deviation (the calculation process is presented in detail in the Ma's report [55]). It can be concluded that ACUM had a slightly narrower pore size distribution than that of CCUM. The membrane surface of ACUM could be modified by the AgNPs, which could fill the membrane pore structure, decreasing the pore diameter.

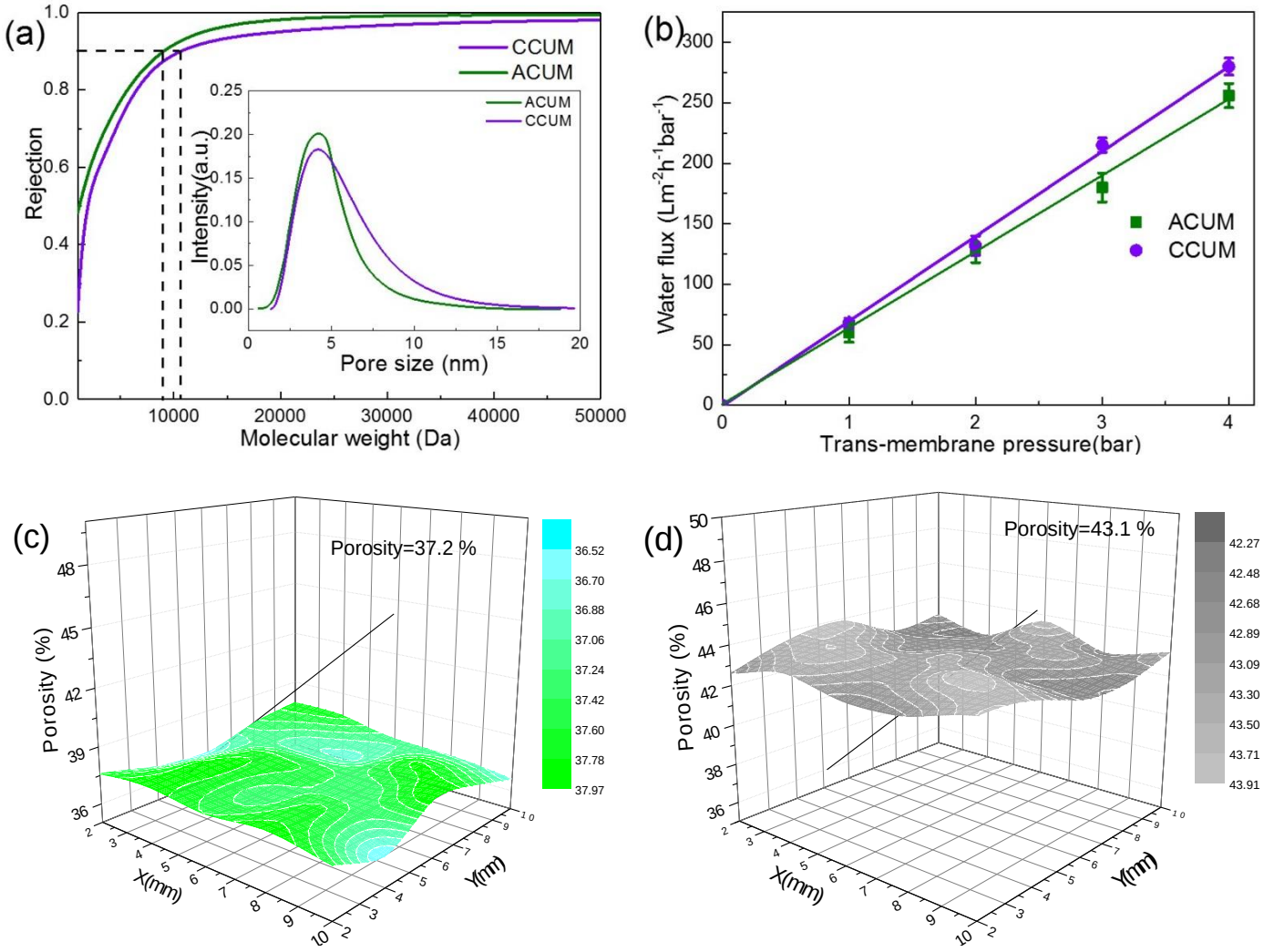


**Fig. 9** (a) Dextran rejection, (b) water flux, and surface porosities of the ceramic UF membranes: (c) ACUM and (d) CCUM.

The pure water fluxes of ACUM and CCUM are shown in **Fig. 9b**. ACUM exhibited a slightly lower permeability (~62 $Lm^{-2}h^{-1}bar^{-1}$) than that of CCUM (~68 $Lm^{-2}h^{-1}bar^{-1}$), as the AgNPs filled membrane pores and decreased the porosity, increasing the separation resistance. To quantitatively measure the porosity of the ceramic UF membrane, a novel method based on ellipsometry was employed to characterize the microstructure (e.g., membrane thickness and refractive index), based on the study by Wessling and Henker [40, 41, 43]. Subsequently, the refractive index was used to calculate the porosity using Equation 1. The surface porosities of ACUM and CCUM were uniform. Their average surface porosities were 37.2% and 43.1%, respectively. **Figs. 9c** and **9d** present surface areas (10 mm × 10 mm) of ACUM and CCUM to show the porosity distributions. The uniform porosity distribution of ACUM reflected the uniform distribution of AgNPs among the membrane material. The measured and calculated parameters are summarized in **Table 1**. The thicknesses of ACUM and CCUM were approximately 1001 and 996 nm, respectively, which is consistent with the above SEM images. The MSE values of the membranes were below 10, indicating the high quality of the fitting [43]. The ellipsometry-based technique can guide further

studies to characterize the surface porosity distributions of ceramic UF and NF membranes.

**Table 1** Ellipsometry analysis of the membranes.

| Membrane | Thickness (nm) | Refractive index ($n_{eff}$) | Porosity (%) | Mean square error (MSE) |
|---|---|---|---|---|
| CCUM | 996 | 1.386 | 43.1 | 7.921 |
| ACUM | 1001 | 1.430 | 37.2 | 8.259 |

### 3.4.3 Comparison of the bonding strengths of CCUM and ACUM

As mentioned in the experimental section, the fabrication of ACUM involved co-sintering process, while CCUM was fabricated by the conventional sintering process. To investigate the effect of the sintering method on the bonding strength between the MF and UF layer, ACUM and CCUM were characterized by a scratch test (**Fig. 10**). The loads of ACUM and CCUM were 59.5 and 56 mN, respectively. The failure occurred at a depth of ~1000 nm, which is consistent with the membrane thickness in **Figs. 10c** and **10d.** In order to investigate the scratching process, the morphologies of the membrane surfaces are shown in **Figs. 10e** and **10f**. The scratch lengths of ACUM and CCUM were similar, consistent with the load forces. The characterization of the scratches demonstrated that the co-sintering process did not negatively affect the mechanical properties, compared with the conventional process, and thus the facile low-cost co-sintering process is very promising for industrial applications.

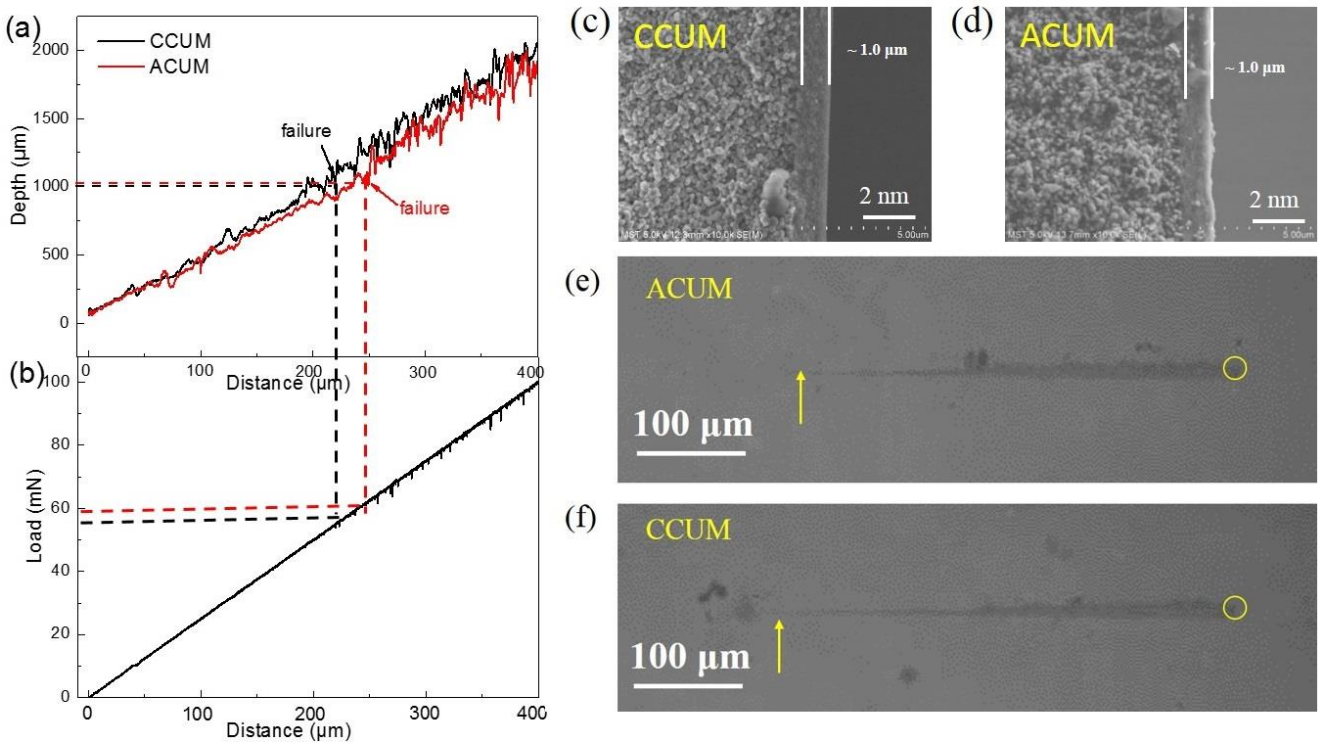


**Fig. 10** Mechanical properties of ACUM and CCUM. (a) (b) Dependences of the depth and load as a function of the distance, (c) (d) cross-section structures of ACUM and CCUM, and (e) (f) microstructures of surface scratches.

### 3.5 Anti-protein-fouling performance

The aim of this study was to fabricate anti-protein-fouling AgNPs-doped ceramic tight membranes and achieve high separation and purification performances. BSA was used for a model protein solution. BSA solutions (pH = 7.4) were prepared to prevent the agglomeration of BSA molecules [56]. **Fig. 11a** shows the protein permeate flux as a function of the filtration time. The permeate flux of the protein solution exhibited a continuous decrease for both ACUM and CCUM. It is worth noting that the final stable permeability of ACUM (30 $Lm^{-2}h^{-1}bar^{-1}$) was higher than that of CCUM (17 $Lm^{-2}h^{-1}bar^{-1}$) although CCUM exhibited a higher pure-water flux (68 $Lm^{-2}h^{-1}bar^{-1}$) than that of CCUM (62 $Lm^{-2}h^{-1}bar^{-1}$). Accordingly, the rejection performances for BSA are shown in **Fig. 11b**. The rejection rate (above 99.5%) of ACUM for BSA was slightly higher than that of CCUM. **Table S1** also shows the concentration of the silver in the permeate solution with the increasing filtration time by ICP tests. It can be seen that there is no obvious silver dissolution in the permeate solution, indicating that AgNPs could be stabilized in the membranes and is appropriate for protein separation.

The surfaces of ACUM and CCUM after the separation of the BSA solution were characterized by SEM (**Fig. 11c**). The ACUM surface had less contaminants than the CCUM surface. The surface of CCUM was covered by contaminants, which significantly decreased the permeability. To further understand the fouling resistances of ACUM and CCUM, the FRRs were calculated as indicators for the degrees of membrane fouling. The membranes were used to filtrate pure water for 60 min and then BSA solution for 60 min. The two steps were considered as one cycle. Subsequently, the membranes were thoroughly washed and a second cycle was carried out. After three cycles, the pure water permeabilities were measured. As shown in **Fig. 11d**, the stable permeabilities of ACUM and CCUM were 49.5 and 24 $Lm^{-2}h^{-1}bar^{-1}$, respectively. The FRRs of ACUM and CCUM were 80% and 35%, respectively, which indicates that ACUM had a better antifouling performance and regeneration performance for BSA molecules.

Usually, the antifouling ability of a ceramic membrane depends mainly on the surface properties such as hydrophilicity–hydrophobicity, membrane roughness, and surface charge [57, 58]. To investigate the antifouling performances of such membranes, their roughnesses and surface charges were investigated. **Fig. 11e** shows the roughnesses of ACUM and CCUM. The roughness of CCUM was approximately 2.6 nm, twice larger than that of ACUM (1.2 nm). The AgNPs toughening properties could provide a smoother membrane surface and thus BSA molecules cannot easily absorb on the membrane surface, compared to the coarser CCUM surface with valleys. The foulants deposited on the membrane surface are referred to as valley clogging [59, 60]. The formed protein layer on the membrane layer could increase the filtration resistance and decrease the water flux. Furthermore, the surface charge of the membrane had a key role in the antifouling performance. **Fig. 11f** shows the zeta potentials of ACUM and CCUM as a function of pH. The AgNPs-doped membrane material exhibited a lower IEP than that of the CCUM membrane material. This indicates that the IEP of the ceramic membrane is controllable, as the AgNPs were more negatively charged at the pH range of 1 to 14 (see **Fig. 4b**, consistent with the Chung's study [23, 25]). The BSA

molecules had an IEP of 4.7 (**Fig. 11**), indicating that the ACUM surface and BSA molecules were also negatively charged at pH = 7.4, providing a strong electronic repulsion of the BSA molecules [61, 62]. However, CCUM had the opposite surface charge at pH = 7.4 to that of BSA, and thus BSA molecules absorbed on the membrane surface and induced a significant membrane fouling. Therefore, ACUM exhibited high antifouling performances in terms of purifications of protein solutions owing to the lower roughness and more negatively charged surface under the test conditions.

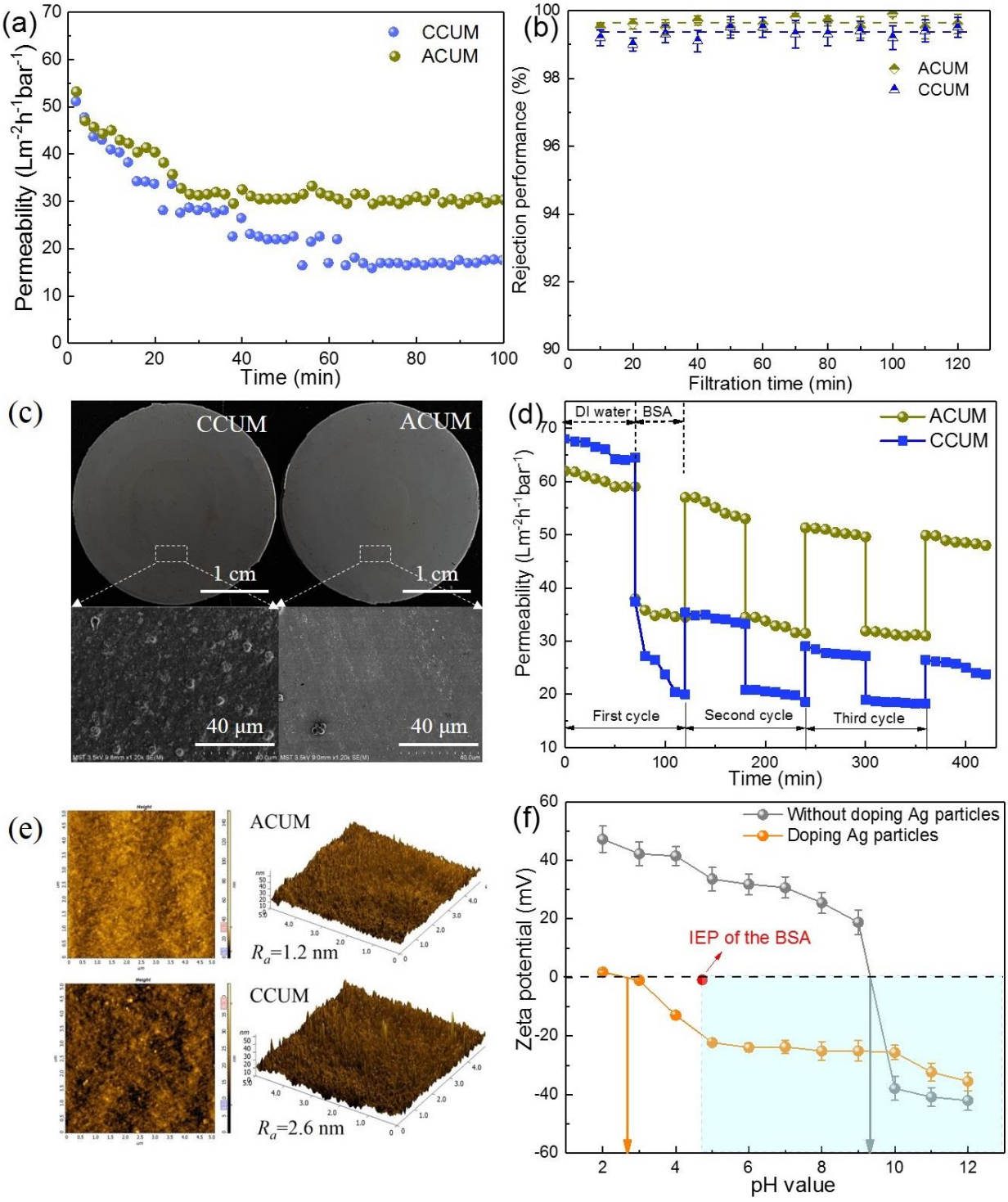


**Fig. 11** BSA separation performances and antifouling analysis of the UF membranes. (a) Permeate fluxes of ACUM and CCUM, (b) BSA rejection performances (trans-membrane pressure: 1 bar; temperature: 25 °C), (c) membrane fouling after the purification of the protein solution, (d) regeneration and anti-protein-fouling performances of the ceramic membranes, (e)

roughness of ACUM and CCUM, and (f) zeta potentials of the membrane materials as a function of pH.

## 4. Conclusions

In this study, ACUMs with better antifouling performances for a BSA solution were fabricated by a facile co-sintering process. A novel boehmite sol with an $AgNO_3$ doping was prepared as the filtration layer material. The effect of the doping content on the performance of the boehmite sol was investigated in detail. The $AgNO_3$ doping content of 5 wt.% could achieve an appropriate surface area and pore diameter, and a complete membrane layer. The AgNPs obtained from silver nitrate not only relieved the sintering stress and toughened the membrane layers in the co-sintering, but also controlled the IEP from positive to negative, providing a better antifouling performance for BSA molecules. The prepared UF membrane with an MWCO of 9000 Da exhibited a pure water permeability of 62 $Lm^{-2}h^{-1}bar^{-1}$ and rejection rate above 99.5 % for BSA molecules. The fabricated ceramic UF membranes exhibited a satisfactory antifouling performance for the BSA solution. After the experimental antifouling cycles, the FRR of ACUM reached 80 %, two times higher than that of CCUM owing to the smoother membrane surface and surface electronic repulsion. This study provided detailed insights on the control of the membrane surface properties by embedding NPs, and their potential application in purifying chemical products.

## Acknowledgements

This work is financially supported by the National Natural Science Foundation of China (91534108, 21808107), Natural Science Foundation of Jiangsu Province (No. BK20180163), National High Technical Research Program of China (2012AA03A606), and the Project of Priority Academic Program Development of Jiangsu Higher Education Institutions (PAPD). We also thank ZHANG Xing (Nanjing Tech University) for his help in characterizing the porosity of the membrane surface by ellipsometry.

## Supporting Information

Supplementary data associated with this article can be found in the online version.

## Reference

[1] M.-J. Corbaton-Baguena, S. Alvarez-Blanco, M.-C. Vincent-Vela, Cleaning of ultrafiltration membranes fouled with BSA by means of saline solutions, Sep. Purif. Technol., 125 (2014) 1-10.

[2] M.J. Lujan-Facundo, J.A. Mendoza-Roca, B. Cuartas-Uribe, S. Alvarez-Blanco, Ultrasonic cleaning of ultrafiltration membranes fouled with BSA solution, Sep. Purif. Technol., 120 (2013) 275-281.

[3] I. Levitsky, Y. Dahan, E. Arkhangelsky, V. Gitis, Retention of modified BSA by ultrafiltration membranes, J. Chem. Technol. Biotechnol., 91 (2016) 400-407.

[4] X. Ke, Y. Huang, T.R. Dargaville, Y. Fan, Z. Cui, H. Zhu, Modified alumina nanofiber membranes for protein separation, Sep.

Purif. Technol., 120 (2013) 239-244.

[5] D. Zou, M.H. Qiu, X.F. Chen, Y.Q. Fan, One-step preparation of high-performance bilayer alpha-alumina ultrafiltration membranes via co-sintering process, J. Membr. Sci., 524 (2017) 141-150.

[6] X. Zhao, R. Zhang, Y. Liu, M. He, Y. Su, C. Gao, Z. Jiang, Antifouling membrane surface construction: Chemistry plays a critical role, J. Membr. Sci., 551 (2018) 145-171.

[7] X. Chen, D. Zou, Y. Lin, W. Zhang, M. Qiu, Y. Fan, Enhanced performance arising from low-temperature preparation of α-alumina membranes via titania doping assisted sol-gel method, J. Membr. Sci., (2018).

[8] S. Bala, D. Nithya, M. Doraisamy, Exploring the effects of graphene oxide concentration on properties and antifouling performance of PEES/GO ultrafiltration membranes, High Perform. Polym., 30 (2018) 375-383.

[9] R. Bi, Q. Zhang, R. Zhang, Y. Su, Z. Jiang, Thin film nanocomposite membranes incorporated with graphene quantum dots for high flux and antifouling property, J. Membr. Sci., 553 (2018) 17-24.

[10] K. Zeng, J. Zhou, Z. Cui, Y. Zhou, C. Shi, X. Wang, L. Zhou, X. Ding, Z. Wang, E. Drioli, Insight into fouling behavior of poly(vinylidene fluoride) (PVDF) hollow fiber membranes caused by dextran with different pore size distributions, Chin. J. Chem. Eng., 26 (2018) 268-277.

[11] X. Li, A. Sotto, J. Li, B. Van der Bruggen, Progress and perspectives for synthesis of sustainable antifouling composite membranes containing in situ generated nanoparticles, J. Membr. Sci., 524 (2017) 502-528.

[12] J. Kim, B. Van der Bruggen, The use of nanoparticles in polymeric and ceramic membrane structures: review of manufacturing procedures and performance improvement for water treatment, Environ. Pollut., 158 (2010) 2335-2349.

[13] L. Yan, Y.S. Li, C.B. Xiang, S. Xianda, Yan, L., Li, Y. S. et al. Effect of nano-sized $Al_2O_3$-particle addition on PVDF ultrafiltration membrane performance. J. Membr. Sci. 276, 162-167, J. Membr. Sci., 276 (2006) 162-167.

[14] A. Bottino, G. Capannelli, A. Comite, Preparation and characterization of novel porous PVDF-$ZrO_2$ composite membranes, Desalination, 146 (2002) 35-40.

[15] P. Jian, H. Yahui, W. Yang, L. Linlin, Preparation of polysulfone–$Fe_3O_4$ composite ultrafiltration membrane and its behavior in magnetic field, J. Membr. Sci., 284 (2006) 9-16.

[16] Y. Cai, D. Wu, X. Zhu, W. Wang, F. Tan, J. Chen, X. Qiao, X. Qiu, Sol-gel preparation of Ag-doped MgO nanoparticles with high efficiency for bacterial inactivation, Ceram. Int., 43 (2017) 1066-1072.

[17] Y. Cai, X. Chen, Y. Wang, M. Qiu, Y. Fan, Fabrication of palladium-titania nanofiltration membranes via a colloidal sol-gel process, Microporous Mesoporous Mater., 201 (2015) 202-209.

[18] Y. Xie, L. Chen, X. Zhang, S. Chen, M. Zhang, W. Zhao, S. Sun, C. Zhao, Integrating zwitterionic polymer and Ag nanoparticles on polymeric membrane surface to prepare antifouling and bactericidal surface via Schiff-based layer-by-layer assembly, J. Colloid Interface Sci., 510 (2018) 308-317.

[19] L. Wang, C. Zhang, F. Gao, G. Mailhot, G. Pan, Algae decorated $TiO_2$/Ag hybrid nanofiber membrane with enhanced photocatalytic activity for Cr(VI) removal under visible light, Chem. Eng. J., 314 (2017) 622-630.

[20] L. Liu, L. Wang, S. Luo, Y. Qing, N. Yan, Y. Wu, Chiral nematic assemblies of silver nanoparticles in cellulose nanocrystal membrane with tunable optical properties, JMatS, 54 (2019) 6699-6708.

[21] M. Irene Lopez-Cazares, F. Perez-Rodriguez, J. Rene Rangel-Mendez, M. Centeno-Sanchez, L.F. Chazaro-Ruiz, Improved conductivity and anti(bio)fouling of cation exchange membranes by AgNPs-GO nanocomposites, J. Membr. Sci., 565 (2018) 463-479.

[22] C.A. Mecha, V.L. Pillay, Development and evaluation of woven fabric microfiltration membranes impregnated with silver nanoparticles for potable water treatment, J. Membr. Sci., 458 (2014) 149-156.

[23] Z. Yang, Y. Wu, H. Guo, X.-H. Ma, C.-E. Lin, Y. Zhou, B. Cao, B.-K. Zhu, K. Shih, C.Y. Tang, A novel thin-film nano-templated composite membrane with in situ silver nanoparticles loading: Separation performance enhancement and implications, J. Membr. Sci., 544 (2017) 351-358.

[24] D.C. Hofmann, J.Y. Suh, A. Wiest, G. Duan, M.L. Lind, M.D. Demetriou, W.L. Johnson, Designing metallic glass matrix composites with high toughness and tensile ductility, Nature, 451 (2008) 1085-1089.

[25] X. Liu, X. Jin, B. Cao, C.Y. Tang, Bactericidal activity of silver nanoparticles in environmentally relevant freshwater matrices: Influences of organic matter and chelating agent, Journal of Environmental Chemical Engineering, 2 (2014) 525-531.

[26] Z. Yang, H. Guo, Z.K. Yao, Y. Mei, C.Y. Tang, Hydrophilic Silver Nanoparticles Induce Selective Nanochannels in Thin Film Nanocomposite Polyamide Membranes, Environ. Sci. Technol., 53 (2019) 5301-5308.

[27] Y. Lin, D. Zou, X. Chen, M. Qiu, H. Kameyama, Y. Fan, Low temperature sintering preparation of high-permeability $TiO_2$/Ti composite membrane via facile coating method, Appl. Surf. Sci., 349 (2015) 8-16.

[28] Y. Lin, Y. Cai, E. Drioli, Y. Fan, Enhancing mechanical and photocatalytic performances on $TiO_2$/Ti composite ultrafiltration membranes via Ag doping method, Sep. Purif. Technol., 145 (2015) 29-38.

[29] X. Cao, J. Ma, X. Shi, Z. Ren, Effect of $TiO_2$ nanoparticle size on the performance of PVDF membrane, Appl. Surf. Sci., 253 (2006) 2003-2010.

[30] D.Y. Zhang, Q. Hao, J. Liu, Y.S. Shi, J. Zhu, L. Su, Y. Wang, Antifouling polyimide membrane with grafted silver nanoparticles and zwitterion, Separation & Purification Technology, (2017).

[31] S.K. Das, M.M. Khan, T. Parandhaman, F. Laffir, A.K. Guha, G. Sekaran, A.B. Mandal, Nano-silica fabricated with silver nanoparticles: antifouling adsorbent for efficient dye removal, effective water disinfection and biofouling control, Nanoscale, 5 (2013) 5549-5560.

[32] H. Basri, A.F. Ismail, M. Aziz, K. Nagai, T. Matsuura, M.S. Abdullah, B.C. Ng, Silver-filled polyethersulfone membranes for antibacterial applications — Effect of PVP and TAP addition on silver dispersion, Desalination, 261 (2010) 264-271.

[33] M.Z. Rong, M.Q. Zhang, W.H. Ruan, Surface modification of nanoscale fillers for improving properties of polymer nanocomposites: a review, Metal Science Journal, 22 (2006) 787-796.

[34] V.M. Gun'Ko, E.F. Voronin, E.M. Pakhlov, V.I. Zarko, V.V. Turov, N.V. Guzenko, R. Leboda, E. Chibowski, Features of fumed silica coverage with silanes having three or two groups reacting with the surface, Colloids & Surfaces A Physicochemical & Engineering Aspects, 166 (2000) 187-201.

[35] M. Qiu, S. Fan, Y. Cai, Y. Fan, N. Xu, Co-sintering synthesis of bi-layer titania ultrafiltration membranes with intermediate layer of sol-coated nanofibers, J. Membr. Sci., 365 (2010) 225-231.

[36] J. Zhu, G. Zhang, G. Liu, Z. Liu, W. Jin, N. Xu, Perovskite Hollow Fibers with Precisely Controlled Cation Stoichiometry via One-Step Thermal Processing, Adv. Mater., 29 (2017).

[37] X. Chen, W. Zhang, Y. Lin, Y. Cai, M. Qiu, Y. Fan, Preparation of high-flux gamma-alumina nanofiltration membranes by using a modified sol-gel method, Microporous Mesoporous Mater., 214 (2015) 195-203.

[38] D. Zou, M.H. Qiu, X.F. Chen, E. Drioli, Y.Q. Fan, One step co-sintering process for low-cost fly ash based ceramic microfiltration membrane in oil-in-water emulsion treatment, Sep. Purif. Technol., 210 (2019) 511-520.

[39] D. Zou, J. Xu, X. Chen, E. Drioli, M. Qiu, Y. Fan, A novel thermal spraying technique to fabricate fly ash/alumina composite membranes for oily emulsion and spent tin wastewater treatment, Sep. Purif. Technol., (2019).

[40] W. Ogieglo, H. Wormeester, K.-J. Eichhorn, M. Wessling, N.E. Benes, In situ ellipsometry studies on swelling of thin polymer films: A review, Prog. Polym. Sci., 42 (2015) 42-78.

[41] W. Ogieglo, H. Wormeester, M. Wessling, N.E. Benes, Spectroscopic ellipsometry analysis of a thin film composite membrane consisting of polysulfone on a porous alpha-alumina support, ACS Appl Mater Interfaces, 4 (2012) 935-943.

[42] D. Zou, X.F. Chen, M.H. Qiu, E. Drioli, Y.Q. Fan, Flux-enhanced α-alumina tight ultrafiltration membranes for effective treatment of dye/salt wastewater at high temperatures, Sep. Purif. Technol., 215 (2018) 143-154.

[43] M.C. Schillo, I.S. Park, W.V. Chiu, H. Verweij, Rapid thermal processing of inorganic membranes, J. Membr. Sci., 362 (2010) 127-133.

[44] W. Chen, M. Wei, Y. Wang, Advanced ultrafiltration membranes by leveraging microphase separation in macrophase separation of amphiphilic polysulfone block copolymers, J. Membr. Sci., 525 (2017) 342-348.

[45] I. Pastoriza-Santos, L.M. Liz-Marzan, Reduction of silver nanoparticles in DMF. Formation of monolayers and stable colloids, Pure Appl. Chem., 72 (2000) 83-90.

[46] I. Pastoriza-Santos, L.M. Liz-Marzán, Formation and Stabilization of Silver Nanoparticles through Reduction byN,N-Dimethylformamide, Langmuir, 15 (1999) 948-951.

[47] D.Y. Zhang, J. Liu, Y.S. Shi, Y. Wang, H.F. Liu, Q.L. Hu, L. Su, J. Zhu, Antifouling polyimide membrane with surface-bound silver particles, J. Membr. Sci., 516 (2016) 83-93.

[48] W. Qin, C. Peng, M. Lv, J. Wu, Preparation and properties of high-purity porous alumina support at low sintering temperature, Ceram. Int., 40 (2014) 13741-13746.

[49] D. Li, H. Wang, W. Jing, Y. Fan, W. Xing, Fabrication of mesoporous $TiO_2$ membranes by a nanoparticle-modified polymeric sol process, J. Colloid Interface Sci., 433 (2014) 43-48.

[50] H. Zhang, G. Wang, D. Chen, X. Lv, J. Li, Tuning Photoelectrochemical Performances of Ag−$TiO_2$ Nanocomposites via Reduction/Oxidation of Ag, Chem. Mater., 77 (2013) 87-95.

[51] S.W. Brittle, D.P. Foose, K.A. O'Neil, J.M. Sikon, J.K. Johnson, A.C. Stahler, J. Ryan, S.R. Higgins, I.E. Sizemore, A Raman-Based Imaging Method for Characterizing the Molecular Adsorption and Spatial Distribution of Silver Nanoparticles on Hydrated Mineral Surfaces, Environ. Sci. Technol., 52 (2018) 2854-2862.

[52] H. Deng, Y. Yu, H. He, Discerning the Role of Ag-O-Al Entities on Ag/gamma-$Al_2O_3$ Surface in NOx Selective Reduction by Ethanol, J. Phys. Chem. C, 119 (2015) 3132-3142.

[53] X. She, M. Flytzanistephanopoulos, The role of Ag-O-Al species in silver–alumina catalysts for the selective catalytic reduction of NOx with methane, J. Catal., 237 (2006) 79-93.

[54] T. Kuzniatsova, M.L. Mottern, K. Shqau, D. Yu, H. Verweij, Micro-structural optimization of supported gamma-alumina membranes, J. Membr. Sci., 316 (2008) 80-88.

[55] X. Ma, P.L. Chen, M. Zhou, Z.X. Zhong, F. Zhang, W.H. Xing, Tight Ultrafiltration Ceramic Membrane for Separation of Dyes and Mixed Salts (both NaCl/$Na_2SO_4$) in Textile Wastewater Treatment, Ind. Eng. Chem. Res., 56 (2017) 7070-7079.

[56] G. Rong, D. Zhou, X. Han, J. Pang, Preparation and characterization of novel zwitterionic poly(arylene ether sulfone) ultrafiltration membrane with good thermostability and excellent antifouling properties, Appl. Surf. Sci., (2017).

[57] D. Rana, T. Matsuura, Surface Modifications for Antifouling Membranes, Chem. Rev., 110 (2010) 2448-2471.

[58] J. Lee, S. Jeong, Y. Ye, V. Chen, S. Vigneswaran, T. Leiknes, Z. Liu, Protein fouling in carbon nanotubes enhanced ultrafiltration membrane: Fouling mechanism as a function of pH and ionic strength, Sep. Purif. Technol., 176 (2017) 323-334.

[59] E.M. Vrijenhoek, S. Hong, M. Elimelech, Influence of membrane surface properties on initial rate of colloidal fouling of reverse osmosis and nanofiltration membranes, J. Membr. Sci., 188 (2001) 115-128.

[60] K. Boussu, B.V.D. Bruggen, A. Volodin, C.V. Haesendonck, J.A. Delcour, P.V.D. Meeren, C. Vandecasteele, Characterization of commercial nanofiltration membranes and comparison with self-made polyethersulfone membranes, Desalination, 191 (2006) 245-253.

[61] X.B. Ke, R.F. Shao, H.Y. Zhu, Y. Yuan, D.J. Yang, K.R. Ratinac, X.P. Gao, Ceramic membranes for separation of proteins and DNA through in situ growth of alumina nanofibres inside porous substrates, Chem. Commun., (2009) 1264-1266.

[62] P. Monash, A. Majhi, G. Pugazhenthi, Separation of bovine serum albumin (BSA) using γ -$Al_2O_3$–clay composite ultrafiltration membrane, J. Chem. Technol. Biotechnol., 85 (2010) 545-554.